

# Hypothesis Testing for Shapes using Vectorized Persistence Diagrams

Chul Moon<sup>\*1</sup> and Nicole A. Lazar<sup>2</sup>

<sup>1</sup>Southern Methodist University

<sup>2</sup>Pennsylvania State University

## Abstract

Topological data analysis involves the statistical characterization of the shape of data. Persistent homology is a primary tool of topological data analysis, which can be used to analyze those topological features and perform statistical inference. In this paper, we present a two-stage hypothesis test for vectorized persistence diagrams. The first stage filters elements in the vectorized persistence diagrams to reduce false positives. The second stage consists of multiple hypothesis tests, with false positives controlled by false discovery rates. We demonstrate applications of the proposed procedure on simulated point clouds and three-dimensional rock image data. Our results show that the proposed hypothesis tests can provide flexible and informative inferences on the shape of data with lower computational cost compared to the permutation test.

*Keywords: Topological Data Analysis, Persistent Homology, Statistical Inference, Hypothesis Testing*

---

<sup>\*</sup>Corresponding author. Email: chulm@smu.edu

# 1 Introduction

Modern science is facing a rapid increase in the volume of data as well as their complexity. Non-standard data types such as functional (Ramsay and Silverman, 2005), manifold (Genovese et al., 2012), and object-oriented (Marron and Alonso, 2014) data have become more common. New methodologies need to be developed to analyze and gain useful information from these data. For example, Figure 1 shows Micro-CT images obtained from two different types of sandstones. The properties of rocks, such as permeability, play an important role in earth science fields, including hydrogeology and petroleum engineering. However, such properties are difficult to estimate; one of the reasons is that they are influenced by parameters linked to pore geometry (Hommel et al., 2018). Because it is not easy to quantify pore geometry, various indirect measures are used instead, such as porosity, tortuosity, and specific surface area (Bernab and Bruderer, 1998; Xiong et al., 2016).

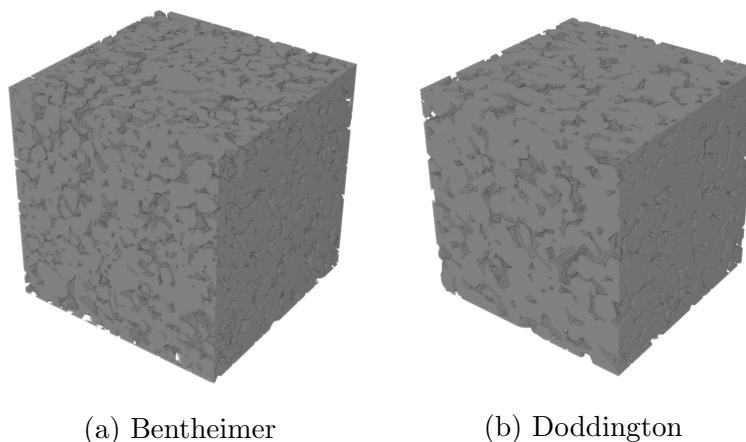


Figure 1: Micro-CT images of Bentheimer and Doddington sandstones (Imperial College London, 2015).

Topological data analysis (TDA) is a recent addition to the analytical toolbox, that quantifies the shape of data using their topological features, such as connected components and holes. A primary TDA tool is persistent homology, which analyzes topological features of data in various scales (Edelsbrunner and Harer, 2008; Carlsson, 2009). Persistent homology provides a numeric descriptor of the shape of data that is robust to noise and insensitive to metrics (Chazal et al., 2017). It has been applied to a wide variety of data

sets, including atomic configurations (Hiraoka et al., 2016), biomolecular structures (Cang and Wei, 2017), brain arteries (Bendich et al., 2016b), and porous materials (Robins et al., 2016).

Using results from TDA, it is possible to move toward statistical inference on the shape of data. For example, by computing persistent homology of the two rocks in Figure 1, we can obtain numeric outputs that describe their shapes, such as size, connectivity, and structure of pores. We can then, in principle, use this output to conduct hypothesis tests to distinguish rock types based on their shapes such as pore shapes and connectivities.

Most statistical and machine learning methods, however, cannot be directly applied to persistent homology results. First, numeric outputs of persistent homology are not vectors. The numeric values that we obtain are sets of intervals that describe how topological features persist. Also, the number of intervals produced differs from dataset to dataset. Therefore, we cannot use approaches developed for symbolic data (Billard and Diday, 2006). Various approaches have been suggested to represent persistent homology results in different spaces while preserving the summarized topological information; in Euclidean space (Bendich et al., 2016a; Adams et al., 2017), reproducing kernel Hilbert space (RKHS) (Reininghaus et al., 2015; Kusano et al., 2016), and  $L^2$ -space (Bubenik, 2015).

Several methods have been proposed to make statistical inference using persistent homology results including confidence interval using bootstrap (Fasy et al., 2014), Bayesian approaches (Maroulas et al., 2019), linear models (Obayashi et al., 2018), and numerical summaries using polynomials (Adcock et al., 2016) and tropical geometry (Kališnik, 2019). There are a few authors who describe hypothesis testing procedures for persistent homology; permutation tests using a pairwise distance of persistence diagrams (Robinson and Turner, 2017; Cericola et al., 2018) and functional summaries (Chen et al., 2015; Berry et al., 2020), multiple hypothesis testing procedures using uniform point cloud data (Vejdemo-Johansson and Mukherjee, 2018), tests using mean persistence landscapes (Bubenik, 2015) and kernel hypothesis tests in RKHS (Kusano, 2019).

In this paper, we propose a two-stage hypothesis test of filtering and testing for persistent homology features represented as vectors in Euclidean space. In the filtering stage, elements that may generate false positives are dropped. In the testing stage, we conduct

multiple hypothesis tests and control the false discovery rate (FDR). Two-stage hypothesis tests in our paper are implemented to reduce false positives whereas they have been used to enhance the detection power for high-dimensional data, including microarray (Hackstadt and Hess, 2009; Tritchler et al., 2009) and genome-wide associations (Murcray et al., 2008; Kooperberg and LeBlanc, 2008).

The rest of the paper is organized as follows. In Section 2, we provide background on persistent homology and issues related to hypothesis tests for vectorized persistence diagrams. Section 3 introduces the proposed two-stage hypothesis test procedures. Section 4 presents the hypothesis testing results for simulated point cloud data and rock image data. Finally, in Section 5, we discuss our main contributions and future directions.

## 2 Topological Data Analysis Background

### 2.1 Homology and Persistent Homology

Consider a shape of interest that is given as a topological space  $\mathcal{X}$ . Homology analyzes  $\mathcal{X}$  by examining its  $k$ -dimensional holes: connected components (zero-dimensional holes), loops (one-dimensional holes), and voids (two-dimensional holes). These  $k$ -dimensional holes are often called the topological features of the space. The  $k$ -th homology group  $H_k(\mathcal{X})$  describes the  $k$ -dimensional holes in  $\mathcal{X}$ . The rank of  $H_k(\mathcal{X})$ , the Betti number  $\beta_k$ , counts the number of  $k$ -dimensional holes. Figure 2 illustrates three spaces and their corresponding Betti numbers.

Persistent homology keeps track of the homology of a sequence of topological spaces. Let  $\emptyset \subseteq \mathcal{X}_0 \subseteq \mathcal{X}_1 \subseteq \dots \subseteq \mathcal{X}_n = \mathcal{X}$  be a non-decreasing sequence of topological spaces. For example, Figure 3 shows a sequence of topological spaces called the Rips complexes  $\mathcal{R}_\epsilon$ . A Rips complex  $\mathcal{R}_\epsilon$  is a set consisting of  $k$ -dimensional simplices, such as vertex, edge, and triangle, where the  $k$ -dimensional simplices correspond to  $k + 1$  points whose pairwise distances are smaller than  $\epsilon$  (Hatcher, 2002).

The inclusion of  $\mathcal{X}_i$  in  $\mathcal{X}_j$  for  $0 \leq i \leq j \leq n$  induces a map called the homomorphism between the homology groups,  $\iota_k(i, j) : H_k(\mathcal{X}_i) \rightarrow H_k(\mathcal{X}_j)$ . Therefore, for a given sequence

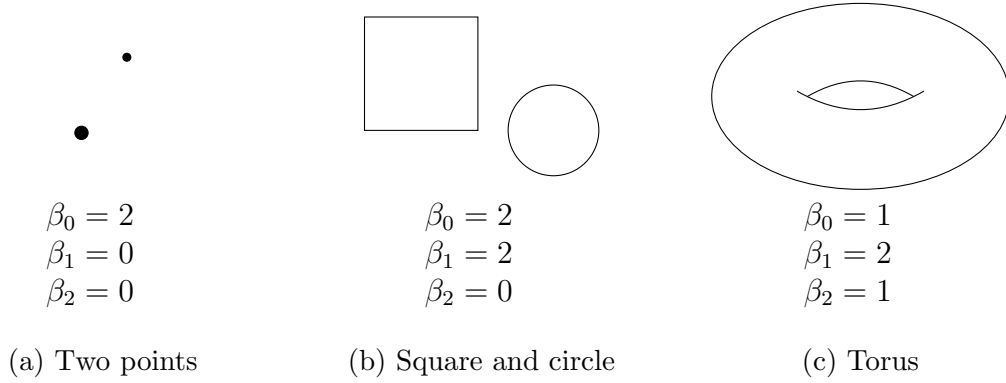


Figure 2: Betti numbers of three topological spaces.  $\beta_0$ ,  $\beta_1$ , and  $\beta_2$  are the number of zero, one, and two dimensional holes in a space. For example, a torus has one connected component, two loops, and one void.

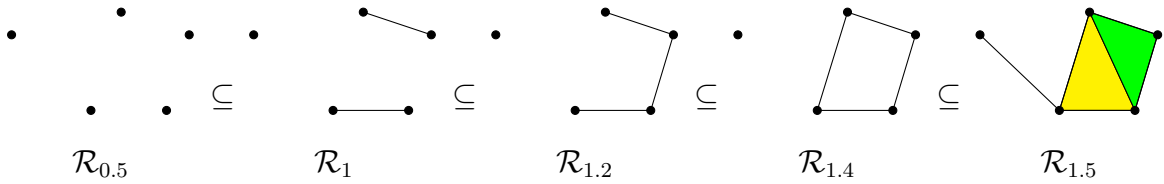


Figure 3: Sequence of Rips complexes. The dots, lines, and colored regions are vertices, edges, and triangles, respectively.

of topological spaces, we have a sequence of homomorphisms

$$0 = H(\mathcal{X}_0) \rightarrow H(\mathcal{X}_1) \rightarrow \cdots \rightarrow H(\mathcal{X}_n) = H(\mathcal{X}).$$

The images of homomorphisms include information about the birth and death of topological features in the sequence of topological spaces. The image of  $\iota_k(i, j)$  includes information of  $k$ -dimensional topological features that appear before  $i$  and disappear after  $j$ . For example, the loop in Figure 3 appears at  $\mathcal{R}_{1.4}$  ( $\epsilon = 1.4$ ) and disappears at  $\mathcal{R}_{1.5}$  ( $\epsilon = 1.5$ ). Information of the loop is included in the image of the dimension one homology group  $\iota_1(i, j)$  where  $1.4 < i < j < 1.5$ .

We define the  $k$ -dimensional  $(i, j)$  persistent homology groups as the image of the homomorphism  $\iota_k(i, j) : H_k(\mathcal{X}_i) \rightarrow H_k(\mathcal{X}_j)$ . The rank of the  $k$ -dimensional  $(i, j)$  persistent homology groups is equal to the number of  $k$ -dimensional topological features at  $\mathcal{X}_j$  that are born at or before  $\mathcal{X}_i$ . Here, the parameter that controls the sequential changes, such as

$i$  or  $j$ , is called the filtration.

From persistent homology, we can observe dynamics of when a specific  $k$ -dimensional hole appears (birth) and disappears (death) over the filtration. As a result, persistent homology is given as multiple intervals of (birth, death).

A persistence diagram is a graphical representation of persistent homology. The (birth, death) intervals are plotted as points in  $\mathbb{R}^2$  of birth ( $x$ -axis) and death ( $y$ -axis). Because the death of a topological feature comes after its birth, points are plotted above the 45-degree line. Figure 4 shows the persistence diagram of the Rips complexes in Figure 3 for dimensions 0 (connected components) and 1 (loops). For example, the blue dots in Figure 4 summarize  $\epsilon$  values when the data points are connected by edges and the red triangle at (1.4, 1.5) in Figure 4 represents the loop created at  $\epsilon = 1.4$ , which dies at  $\epsilon = 1.5$ .

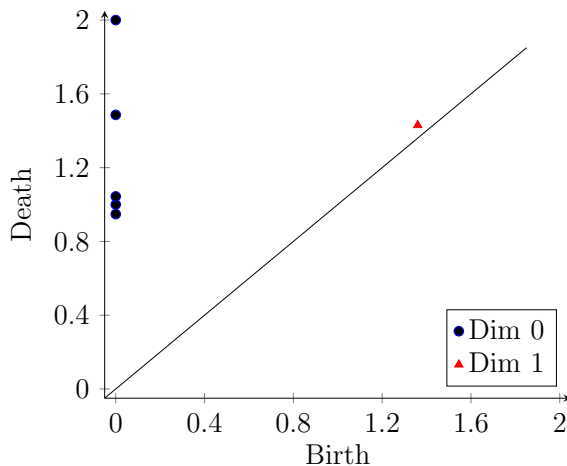


Figure 4: Dimension 0 and 1 persistence diagram of Rips complexes in Figure 3

Persistent homology can explore different aspects of shapes when it is applied to different types of data. For example, when persistent homology is computed for the binary rock images, it can describe geometric properties or materials such as sizes of pores and grains, their connectivity, and pore-throat radius (Robins et al., 2016). Figure S1 and S2 in Supplementary Material show examples of topological features of two-dimensional binary rock images and where such features appear in dimension 0 and 1 persistence diagrams.

For more detailed explanation of persistent homology, see Hatcher (2002), Edelsbrunner and Harer (2008), and Ghrist (2008).

## 2.2 Vectorized Persistence Diagrams in Euclidean Space

Although persistence diagrams include information about topological features, it is difficult to use them as input in data analysis. This is because persistence diagrams are not numeric vectors, which most classical statistical and machine learning methods require. Ways to represent persistence diagrams as vectors include binning (Bendich et al., 2016a) and persistence images (Adams et al., 2017) in Euclidean space, persistence scale-space kernel (Reininghaus et al., 2015) and persistence weighted Gaussian kernel (Kusano et al., 2016) in RKHS, rank function (Robins and Turner, 2016) and persistence landscapes (Bubenik, 2015) in  $L^2$  space.

The vector representation of persistence diagrams in Euclidean space has some advantages. First, the representation in Euclidean space makes it easier to conduct prediction and classification by applying classical statistical models and machine learning methods such as regression and support vector machine (Adams et al., 2017; Obayashi et al., 2018). Second, it has a natural graphical summary unlike the other representations.

Bendich et al. (2016a) suggest a binning method for a Euclidean vector representation. First, a persistence diagram  $PD = \{(\text{birth}, \text{death})\}$  is transformed into  $P = \{(\text{birth}, \text{death} - \text{birth})\}$ . The transformed persistence diagrams are divided into a pre-determined number of bins. Then the number of topological features (points in persistence diagrams) included in each bin is counted and recorded as intensity values. However, the binning method is a stable vector representation of persistent diagrams; small changes in persistence diagrams may result in different vector representations.

Adams et al. (2017) propose a different robust vectorization method called the persistence image. First, a persistence diagram  $PD = \{(\text{birth}, \text{death})\}$  is transformed into  $P = \{(\text{birth}, \text{death} - \text{birth})\}$ , as before. With smoothing function  $f_{(u,v)}$  for  $(u, v) \in P$  and weight function  $w$ , the persistence surface  $\rho_P$  of the transformed persistence diagram  $P$  is

$$\rho_P(x, y) = \sum_{(u,v) \in P} f_{(u,v)}(x, y) \cdot w(u, v),$$

where  $x$  and  $y$  are the  $(x, y)$ -coordinates of the persistence surface. The persistence images are obtained by taking an integral of  $\rho_P$  over a given grid. Adams et al. (2017) show that the persistence image is stable with respect to bottleneck and Wasserstein distances

(Edelsbrunner and Harer, 2010). In this paper, we use persistence images to represent persistence diagrams as vectors in Euclidean space.

The smoothing and weight functions are selected to preserve information in the persistence diagrams. We use the Gaussian smoothing function  $f_{(u,v)}(x, y|h) = \frac{1}{2\pi h^2} \exp(-((x - u)^2 + (y - v)^2)/2h^2)$  with  $h = 1.5 * (\text{grid size})$ . One can choose different values of  $h$ , but the persistence image representation is robust to the choice of the variance of the Gaussian function (Adams et al., 2017). Table 1 summarizes the four weights we use in this paper. The linear weight assigns higher weights to persistent topological features whereas the constant weight gives equal weights to all features. The soft(hard) arctangent weight is closer to the constant(linear) weight. The arctangent weights are suggested in Kusano et al. (2016) for RKHS and extended to persistence images in Obayashi et al. (2018).

Name	Weight
Constant	$w(u, v) = 1$
Soft arctangent	$w(u, v) = \arctan(0.5(v)^{0.5})$
Hard arctangent	$w(u, v) = \arctan(v)$
Linear	$w(u, v) = v$

Table 1: Summary of the four weights. Here,  $(u, v)$  are birth and death values in a transformed persistence diagram  $P$ .

Figure 5 illustrates the conversion steps from the persistence diagram to the persistence image. First, the (birth, death) pair is transformed to (birth, death–birth). Then the transformed persistence diagram is represented as the persistence image by using a smoothing function and a weight.

### 2.3 Hypothesis Tests for Persistent Homology

One can consider a hypothesis test that compares the topological features of data using persistence diagrams. However, it is difficult to define probability distributions on the space of persistence diagrams because the space is infinite in dimension and has complicated geometry (Robinson and Turner, 2017). As a result, the hypothesis test methods for

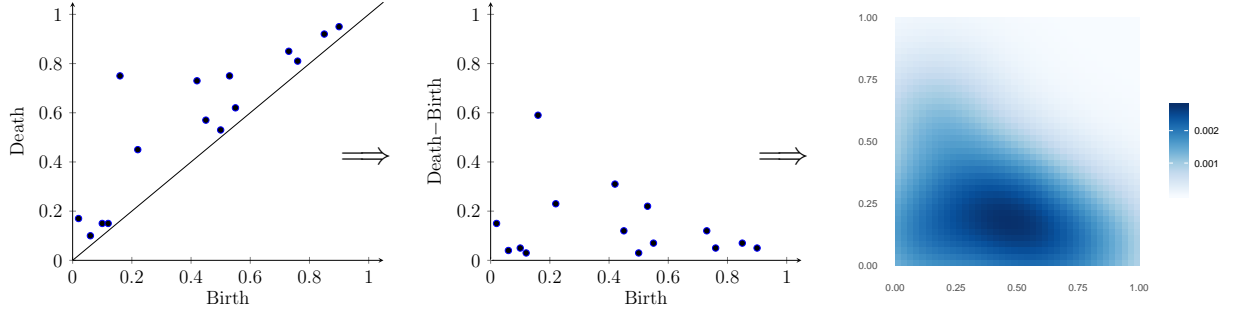


Figure 5: Steps of converting the persistence diagram into the persistence image. From the original persistence diagram (left) to the transformed persistence diagram (middle) to the persistence image (right). In this example, Gaussian smoothing function and soft arctangent weight are used for the persistence images.

persistent homology have been studied in two ways: using permutations and represented persistence diagrams.

First, the permutation-based tests are defined on the space induced by pairwise metrics of persistence diagrams and functional spaces. Robinson and Turner (2017) propose a permutation test for a two-sample setting using persistence diagrams. Assume that we have persistence diagrams  $PD_i$ ,  $i \in \{1, 2, \dots, n\}$  obtained from two groups of size  $n_1$  and  $n_2$  ( $n_1 + n_2 = n$ ). Let  $G = \{I, J\}$  be labels for the two groups where  $I, J \subset \{1, 2, \dots, n\}$ ,  $I \cap J = \emptyset$ ,  $I \cup J = \{1, 2, \dots, n\}$ ,  $n(I) = n_1$ , and  $n(J) = n_2$ . The permutation test uses a joint loss function  $L$  of a label  $G$  defined by

$$L(G = \{I, J\}) = \frac{2}{n_1(n_1 - 1)} \sum_{i < j \in I} d(PD_i, PD_j) + \frac{2}{n_2(n_2 - 1)} \sum_{i < j \in J} d(PD_i, PD_j),$$

where  $d$  is a pairwise distance function for persistence diagrams such as bottleneck or Wasserstein distance. The joint loss value measures the similarity of persistence diagrams within groups. If persistence diagrams within groups are similar(different) to each other, then the joint loss value will be small(large). Algorithm S1 in Supplementary Material presents the permutation test procedure of Robinson and Turner (2017). Cericola et al. (2018) extend the two-sample test scheme to multiple label group testing using the one-way analysis of variance (ANOVA) procedure and Vejdemo-Johansson and Mukherjee (2018) propose procedures to control the multiple testing problem. Also, Chen et al. (2015) and Berry et al. (2020) propose permutation tests using functional representations of persistence

diagrams.

Second, hypothesis tests are conducted to the various persistence diagram representations. Bubenik (2015) suggests various tests for persistence landscapes such as two-sample tests for mean persistence landscapes and Hotelling’s  $T^2$  test. Kusano (2019) applies the two-sample kernel test of Gretton et al. (2006, 2012) to persistence diagram representations using the persistent weighted Gaussian kernel.

Existing hypothesis test approaches have some limitations. First, the computational costs for the permutation test using persistence diagrams are high. Computing pairwise distances for persistence diagrams is computationally expensive;  $O(n_f^{1.5} \log n_f)$  for bottleneck distance (Kerber et al., 2017) and  $O(n_f^3)$  using the Hungarian algorithm (Munkres, 1957) and  $O(n_f^\alpha)$  using the auction algorithm (Kerber et al., 2017) for Wasserstein distance, where  $n_f$  is the number of features in the persistence diagrams and  $\alpha$  is determined by approximation. Second, most hypothesis test methods except for the persistence landscape do not provide information on how each topological feature contributes to any observed differences. Therefore, it is difficult to identify which features play an essential role in the hypothesis test. Lastly, some methods do not provide an option for assigning weights to topological features that enables flexible interpretation. For example, the permutation test using persistence diagrams and the hypothesis test using persistence landscapes are only available under the fixed linear weight.

Conducting a hypothesis test on persistence images can overcome the limitations; it can be performed with low computational cost, identify topological features that account for the differences, and implement weights. However, a naive application of hypothesis tests to persistence images can lead to an incorrect conclusion.

## 2.4 Naive Hypothesis Test for Persistence Images

For the vectorized persistence diagrams in Euclidean space, we can measure the differences by comparing the mean values of vectors. We consider testing the difference between two groups of spaces ( $\mathcal{X}_1$  and  $\mathcal{X}_2$ ) for simplicity. It is straightforward to generalize the approach to more than two groups, similar to the transition from t-tests to ANOVA. Assume that  $n_1$  and  $n_2$  persistence diagrams are obtained from  $\mathcal{X}_1$  and  $\mathcal{X}_2$ , respectively. Let  $x_{(j,k)}^i$  be

the  $i$ th element of group  $j$ 's  $k$ th persistence image, where  $i \in \{1, \dots, m\}$ ,  $j = 1, 2$ , and  $k \in \{1, \dots, n_j\}$ . Also, let  $\mu_j^i = E_k(x_{(j,k)}^i)$  be the mean of the  $i$ th element of group  $j$ 's persistence images. Then, the hypotheses for testing differences between two persistence images are

$$\begin{aligned} H_0 : \quad & \mu_1^i = \mu_2^i \text{ for all } i \in \{1, \dots, m\} \\ H_1 : \quad & \mu_1^i \neq \mu_2^i \text{ for at least one } i \in \{1, \dots, m\}. \end{aligned}$$

However, it is not appropriate to implement these naive hypotheses directly. First, not all areas of the persistence images are equally interesting. There will most likely be multiple elements with a mean close to zero in both groups just because they are far from the diagonal or are in otherwise sparse regions. Second, the elements are not independent. The persistence image uses a smoothing function, so nearby elements can be dependent.

To illustrate these issues, we reproduce a simulation study considered in Robinson and Turner (2017). We randomly sample 100 sets of 50 points from each of two different shapes: one circle of radius 1 (shape 1) and two circles of radius 0.9 and 1.1 (shape 2), as shown in Figure 6. We compute persistent homology for 200 sets of point cloud data using the Rips complex. The difference between the two spaces is reflected in the one-dimensional persistence diagrams, given in the second from the right panel of Figure 6. The dimension one interval for shape 1 (Death – Birth  $\approx 1.3$ ) is longer than the longest dimension one interval for shape 2 (Death – Birth  $\approx 1.1$ ). Also, shape 2 has several very short-lived dimension one intervals. The 200 one-dimensional persistence diagrams are converted to 200 persistence images.

We conduct naive two-sample pooled variance  $t$ -tests at every element to test the differences between the two spaces. Figure 7 presents the average difference of the persistence images, standard errors, and two-sample  $t$ -test statistics.

As shown in the Figure, some elements which have small mean differences in Figure 7a correspond to large  $t$ -test statistics in Figure 7c (i.e., elements on the top). This happens because the corresponding elements have small standard errors. For example, the elements on the top-left corner in Figure 7c have large test statistics because the sample standard deviations are relatively small. As a result, it is difficult to differentiate whether the large test statistics are due to the mean differences or the small sample standard errors.

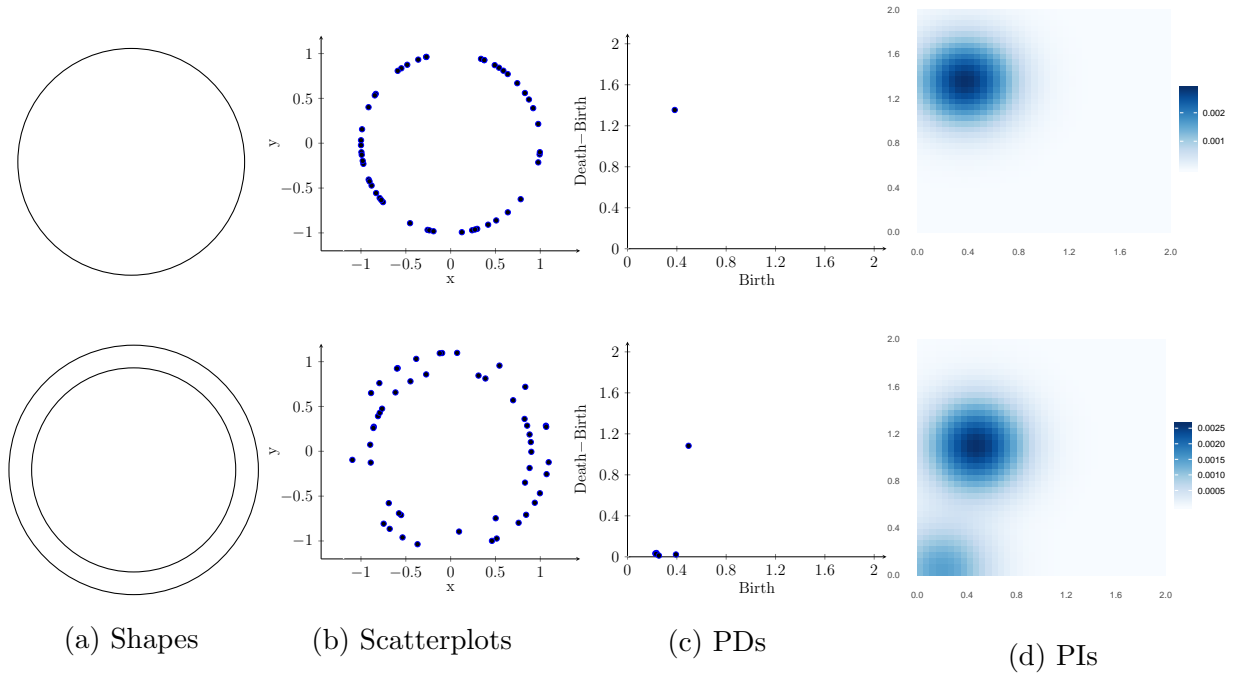


Figure 6: (a) Two shapes, (b) scatterplots of 50 randomly sampled points, (c) transformed one-dimensional persistence diagrams, and (d) persistence images. We use the Gaussian smoothing function with the soft arctangent weight for the persistence images.

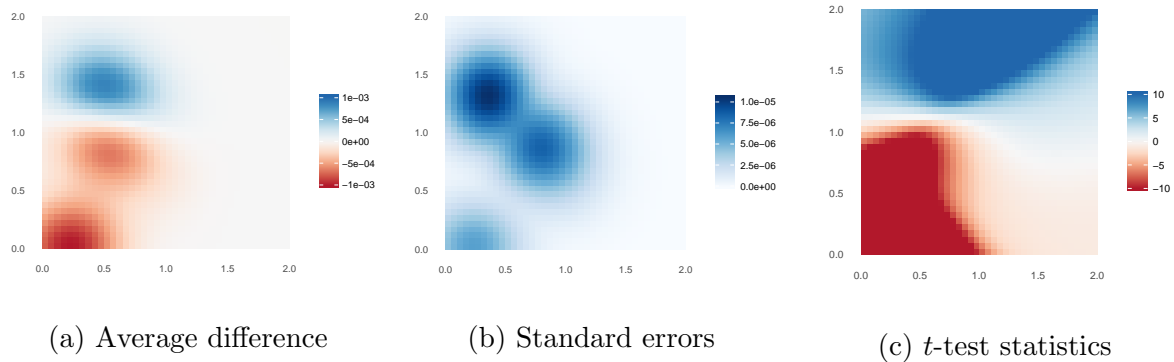


Figure 7: Average differences of one-dimensional persistence images, standard errors, and  $t$ -test statistics. The  $t$ -test statistics less than -10 and greater than 10 are plotted as -10 and 10, respectively.

The elements with small mean differences having large test statistics can be seen as the false positives in this case. The actual differences of the shapes will appear around the three peak areas in Figure 7a and 7b. Even though the mean difference of one element

is negligibly small compared to other elements, the  $t$ -test statistic can still be large if its standard error is small enough. These false positives are closely related to the vectorization process; once persistence diagrams are vectorized, the local element loses the information about the overall variability. Therefore, overall mean or variability information should be considered for the hypothesis testing of persistence images.

Also, when we test multiple hypotheses simultaneously, the multiple testing problem arises. Failure to adjust for multiple testing can lead to an increase of false positives. The multiple testing adjustments such as the family-wise error rate (Hochberg and Tamhane, 1987) and false discovery rate (Benjamini and Hochberg, 1995) aim to control the rate of false positives while maintaining statistical power.

The adjusted multiple hypothesis results need to be robust under dependency among elements in persistence images. Most multiple testing adjustment methods assume independence between tests (Benjamini and Hochberg, 1995; Storey, 2002), whereas some methods control the error rates under various types of dependence (Benjamini and Yekutieli, 2001; Fan et al., 2012). It is necessary to consider potential dependence structures of persistence images in the multiple testing adjustments.

In the next section, we suggest a hypothesis testing approach for persistent images to handle false positives and adjust multiple tests under dependence.

### 3 Two-stage Hypothesis Test Procedures

The suggested hypothesis test approach consists of two stages: filtering and testing. We use two independent statistics (filter and test statistics) in the two stages.

**Stage I: Filtering** The idea of filtering variables has been proposed to increase power for high-dimensional data (McClintick and Edenberg, 2006; Hackstadt and Hess, 2009; Mieth et al., 2016). When the variables are filtered, the number of variables being tested is reduced. As a result, filtering could potentially lead to an increase in the number of discoveries after multiple testing corrections. Unlike the way in which filtering has been used in the previous literature, the two-stage procedure in this paper is implemented to drop elements that are noninformative or more likely to be false positives. Therefore, the

overall power may not increase after filtering in this instance.

We add one additional step of removing unnecessary elements in the upper-right corner of the transformed persistent diagram prior to filtering. This part of the image corresponds to an empty area in most persistence diagrams and hence contributes nothing to the inference.

Bourgon et al. (2010) show that false positive rates are not maintained for a two-stage procedure if inappropriate filter statistics are used. More specifically, a filter statistic needs to be independent of the test statistic because the null distribution in the second stage is a conditional distribution given the filter statistic. For example, Bourgon et al. (2010) use the overall sample mean and standard deviation, and Guo and Romano (2017) use a sum of squared values as filter statistics for  $t$ -test statistics.

In this paper, we use the overall sample mean  $\bar{X}^i$  and overall sample standard deviation  $s^i$  as filter statistics separately for each element  $i$ . For a given threshold  $C$ , elements whose filter statistics are less than the  $C^{th}$  percentile are removed.

One of the disadvantages of the two-stage hypothesis testing is that the choice of the filtering threshold  $C$  could be subjective (Du and Zhang, 2014). Ignatiadis et al. (2016) suggest a data-driven greedy independent filtering procedure that chooses the threshold that maximizes the number of discoveries among all possible candidates. However, this approach is not relevant in our setting because our objective with filtering is to avoid global false positives, not to increase detection power. We examine the effect of the choice of filtering threshold in Section 4.1.1 and discuss other possible approaches in Section 5.

**Stage II: Testing** In the second stage, we conduct hypothesis tests on the remaining elements and adjust for multiplicity. Though we use the pooled-variance  $t$ -test in our analysis, any other standard approach can be used such as unpooled  $t$ -test, nonparametric two-sample tests, ANOVA, and nonparametric ANOVA (Bourgon et al., 2010).

The effects of the dependence of tests on multiple test adjustment methods have been studied including positive regression (Benjamini and Yekutieli, 2001), random correlation structure (Kim and van de Wiel, 2008) and block-correlation structure (Stevens et al., 2017). We assume that the elements in persistence images have a block-correlation structure: the elements within blocks have the same correlation coefficients so that the correlation between

the elements  $i \neq j$ ,

$$\rho_{i,j} = \begin{cases} \rho, & \text{if } B_i = B_j \\ 0, & \text{otherwise} \end{cases}$$

where  $B_k \in \{1, 2, \dots, B\}$  is the block that the element  $k$  belongs to and  $B$  is the total number of blocks. In persistence images, the elements around peaks can be considered as blocks. According to Stevens et al. (2017), the adaptive procedure of Benjamini and Hochberg (2000), the q-value method of Storey (2002), and the two-stage procedure of Benjamini et al. (2006) well control the FDR regardless of the effect size and degree of correlation under the block-correlation settings. In this paper, we use the q-value method of Storey (2002). The q-value is an infimum of a positive false discovery rate (pFDR),

$$pFDR = E(V/R | R > 0),$$

where  $V$  is the number of false positives and  $R$  is the number of the hypotheses whose test statistics are in the critical region. The q-values are analogous to the p-values in terms of pFDR (Storey, 2002).

Algorithm S2 in Supplementary Material summarizes the suggested testing procedure.

## 4 Results

### 4.1 Point Cloud Simulation

#### 4.1.1 Effect of Filtering Threshold and Weight

We simulate point clouds from the two shapes of Figure 6. First, we randomly draw 10 point clouds of 50 points on shape 1 (one circle) and add noise that follows  $N(0, \sigma^2)$ . Then, we apply the same sampling procedure for shape 2 (two different-sized circles). These 20 point clouds, ten from each shape, are used to conduct one hypothesis test. We repeat this 500 times for a given  $\sigma = 0.05, 0.1, 0.15, \text{ and } 0.2$ .

We construct the Rips complex separately for each of the  $20 * 500 * 4 = 40,000$  point clouds and compute persistence homology using the TDA package in R (Fasy et al., 2019). The one-dimensional persistence diagrams are converted into persistence images of 40 by

40 elements using a Gaussian kernel with a smoothing parameter  $h = 0.075$ . We conduct both the naive and two-stage hypothesis tests.

**Effect of Filtering Threshold** We use five filtering thresholds  $C = 0\%$ ,  $20\%$ ,  $40\%$ ,  $60\%$  and  $80\%$  to investigate the effect of  $C$ . Figure 8 shows the q-values of one simulation dataset of  $\sigma = 0.05$  for the five filtering thresholds when overall sample standard deviations are used as filter statistics. Figure S3 in Supplementary Material shows the q-values when we use the overall sample means as filter statistics.

Filtering could remove the potential false positive and sparse regions. In Figure 8, one of the areas that might be related to false positives is between  $(1,0)$  to  $(2,0)$ ; the region that has small mean differences but has small standard errors as Figure 7. The potential false positive region starts to be filtered out when the threshold reaches  $20\%$ . Also, regions that correspond to sparse areas in the persistence diagrams are filtered out.

The filtering may not lead to an increase in power, as explained in Section 3. If the filtered noninformative elements correspond to large test statistics, then overall power may decrease. Tables S1, S2, S3, and S4 in Supplementary Material show the power of the two-stage two-sample  $t$ -tests under  $\alpha = 0.05$  for the q-value test adjustment procedure, two filter statistics (overall sample mean and standard deviation), five filtering thresholds ( $0\%$ ,  $20\%$ ,  $40\%$ ,  $60\%$ , and  $80\%$ ), five noise levels ( $0$ ,  $0.05$ ,  $0.10$ ,  $0.15$ , and  $0.20$ ), and four weights (constant, soft arctangent, hard arctangent, and linear). In most cases, positive thresholds have larger powers than no filtering ( $C = 0\%$ ). However, when too many elements are filtered out by using a large threshold (e.g.,  $C = 80\%$ ), then power decreases.

**Effect of Weight** We compare four weights (constant, soft arctangent, hard arctangent, and linear) used in the vectorization procedure. The latter two (linear and hard arctangent) tend to assign higher weights to persistent features (i.e., points that are far from the 45-degree line in the persistence diagrams). On the other hand, the first two (constant and soft arctangent) give similar weights to features regardless of their persistence.

Figure 9 compares the powers of two-stage vectorized hypothesis tests with filtering threshold  $C = 50\%$  under these four weights to the permutation test of Robinson and Turner (2017). For the permutation test, pairwise distances between persistence diagrams

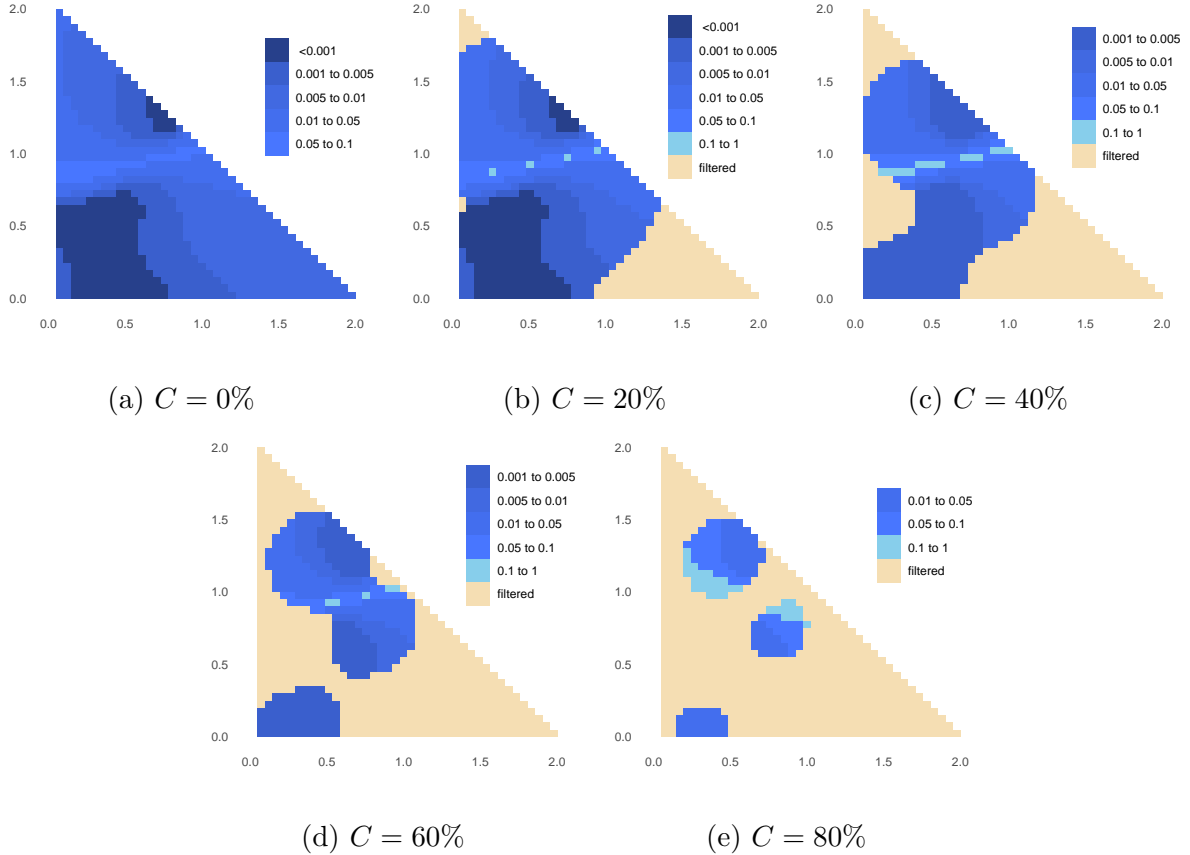
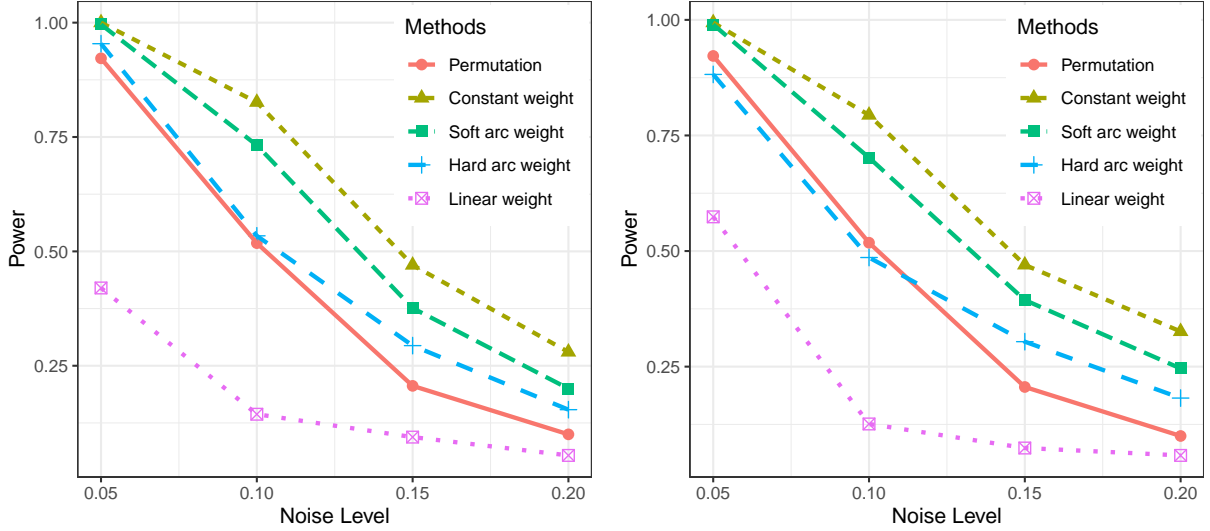


Figure 8: q-values of two-stage hypothesis tests with five threshold values. Overall sample standard deviation is used as a filter statistic.

are measured by the Wasserstein distance. We see that the two-stage hypothesis tests with the constant and soft arctangent weights achieve higher power than the permutation tests of Robinson and Turner (2017) whereas the linear weight shows lower power. Also, the increase in power over the permutation test is better for higher levels of noise. Similar patterns are seen for either choice of filter statistic.

The results imply that the proposed two-stage test provides flexible options to compare the differences between collections of persistence diagrams. The pairwise distances tend to assign small distances for differences of topological features that are close to the 45-degree line, similar to the linear or hard arctangent weights. Therefore, computing the pairwise distances in permutation tests is comparable to measuring differences between persistence images with the linear or hard arctangent weights. In our simulated datasets, points close to



(a) Filter statistics: sample mean

(b) Filter statistics: sample standard deviation

Figure 9: Powers at significance level  $\alpha = 0.05$  and filtering threshold  $C = 50\%$ .

the 45-degree line in the persistence diagrams play an important role in differentiating the two groups. As a result, the permutation tests and two-stage tests using hard arctangent and linear weights do not perform well capturing such differences compared to the tests using the constant and soft arctangent weights.

#### 4.1.2 Effect of Persistence Image Resolution

We next examine the effect of the resolution of the vectorized persistence diagrams on inference. A point cloud of 50 points is sampled from each shape of Figure 6 and repeated 50 times so that  $n_1 = n_2 = 50$ . For simplicity, Gaussian noise is not added in this simulation.

The  $50 * 2 = 100$  one-dimensional persistence diagrams are converted into persistence images at four different resolutions: 20 by 20, 40 by 40, 60 by 60, and 80 by 80. We use the Gaussian kernel with smoothing parameters set to be 1.5 times the size of the pixel ( $h = 0.15, 0.075, 0.05, \text{ and } 0.0375$ , respectively). Also, the soft arctangent weight is used. We use overall standard deviation as a filter statistic and pooled-variance  $t$ -statistic as a test statistic for the two-stage hypothesis tests. The filtering threshold is set to be  $C = 50\%$  and  $q$ -values are used to adjust multiple test results.

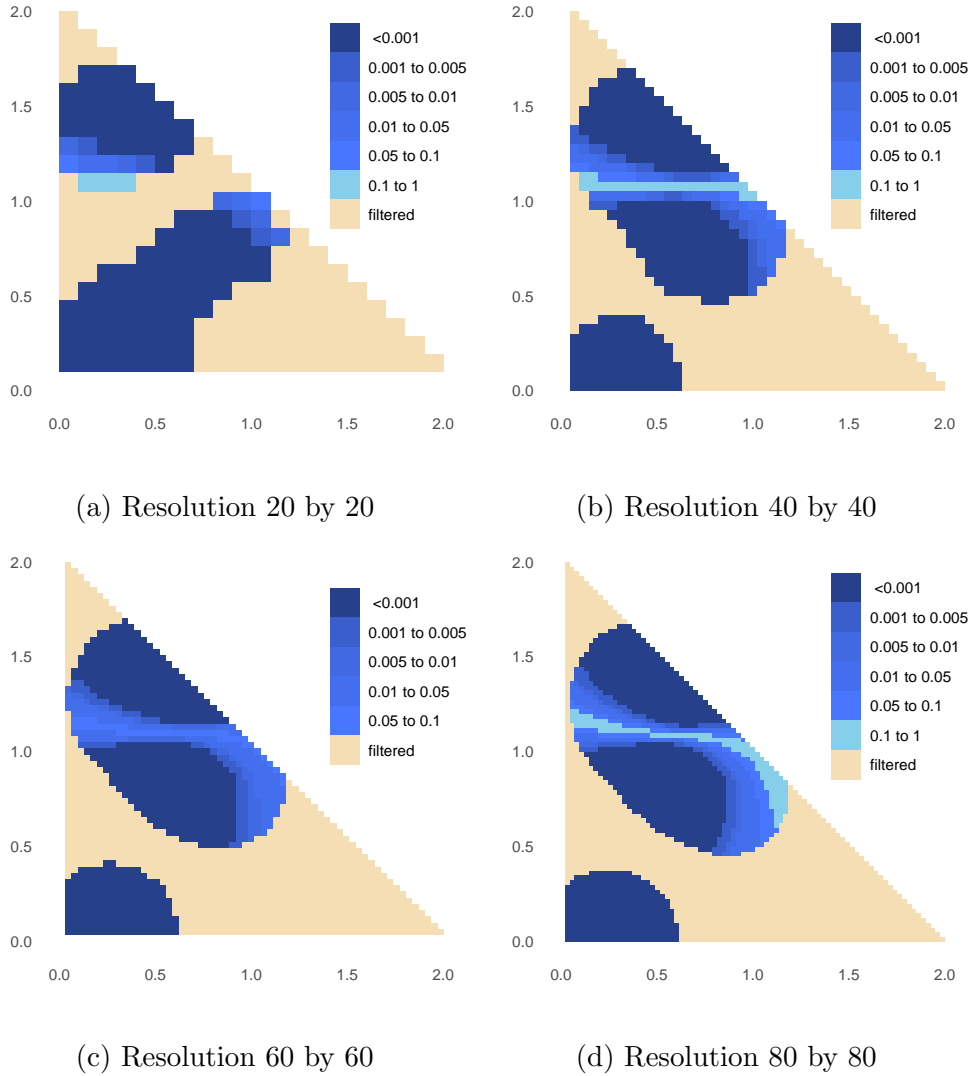


Figure 10: q-values at four different resolutions.

Figure 10 illustrates the filtered elements and q-values for the tested elements. We see that the q-values are similar to each other except for the case of 20 by 20 resolution. These results suggest that the two-stage hypothesis tests are robust to the resolution of the vectorized persistence diagrams unless the resolution is too coarse. The persistence image of resolution 20 by 20 does not filter out the elements in the middle, unlike the other higher resolution persistence images. The variability of regions in the middle is affected by the neighboring elements because a relatively large smoothing parameter is used for 20 by 20 resolution images.

## 4.2 Two-dimensional Binary Image Simulation

We compare two-dimensional random binary images generated by Algorithm 1 of Obayashi et al. (2018). Three sets of parameters are used to generate images:  $(M = 180, S = 80)$ ,  $(M = 190, S = 75)$ , and  $(M = 200, S = 70)$ , where  $M$  is the number of seed points and  $S$  is the number of dispersion points. For all settings, we set dispersion scales  $\sigma_1 = \sigma_2 = 4$  and threshold  $t = 0.7$ . Figure 11 shows examples of generated binary images from each parameter set. The simulated images can be considered as pseudo-rock images. Differences between the images are not easily identifiable by visual inspection.

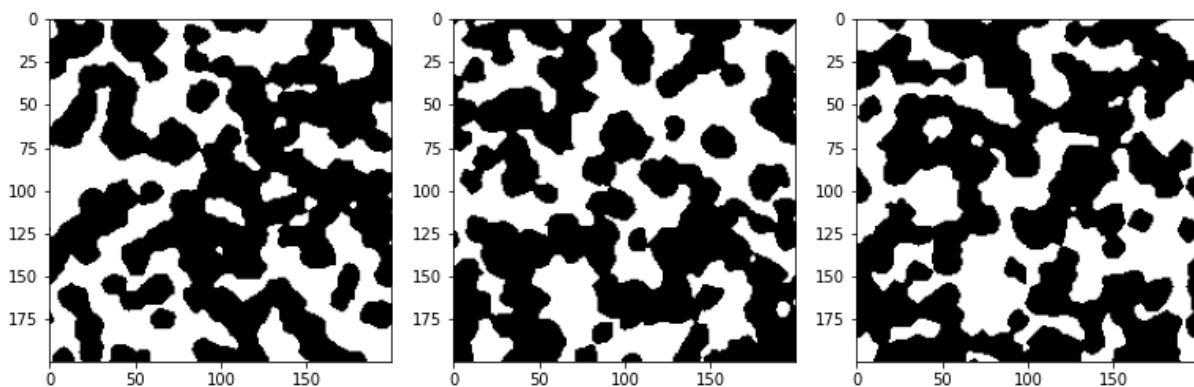


Figure 11: Examples of two-dimensional pseudo-rock images with parameters  $(M = 180, S = 80)$  (left),  $(M = 190, S = 75)$  (center), and  $(M = 200, S = 70)$  (right).

Hypothesis tests are conducted using topological features of the binary images. We consider three scenarios to compare the pseudo-rock images: scenario 1 examines two groups of  $(M = 180, S = 80)$  images, scenario 2 compares  $(M = 180, S = 80)$  and  $(M = 190, S = 75)$  groups, and scenario 3 tests  $(M = 180, S = 80)$  and  $(M = 200, S = 70)$  groups. All groups in each scenario include 50 images of size 200 by 200. The images are transformed using a Signed Euclidean Distance Transform (SEDT) procedure (Robins et al., 2016). Then, cubical cell complexes are constructed according to the SEDT values. Persistent homology is computed using the GUDHI library (Dlotko, 2015). For the permutation test,  $N = 200$  repetitions are used. For two-stage hypothesis tests, we use the persistence images converted using the four weights and overall mean filter statistic and threshold  $C = 50\%$ .

The hypothesis test results show that they can differentiate the simulated binary images based on their topological features. Table 2 shows minimum q-values from two-stage

hypothesis tests and p-values from permutation tests. The case of the largest parameter differences, scenario 3, yields the smallest q-values and p-values.

		Scenario 1		Scenario 2		Scenario 3	
		Dim 0	Dim 1	Dim 0	Dim 1	Dim 0	Dim 1
Two-stage test	Linear	0.717	0.998	0.235	0.135	0.034	0.018
	Hard	0.679	0.992	0.207	0.277	0.007	0.012
	Soft	0.719	0.982	0.168	0.220	0.004	0.009
	Constant	0.763	0.798	0.121	0.792	0.003	0.019
Permutation test		0.520	0.700	0.090	0.475	0.000	0.000

Table 2: Minimum q-values of two-stage tests and p-values of permutation tests.

### 4.3 Three-dimensional Sand Pack Image Data Analysis

We analyze two sand packs: F42 (unground silica, US Silica Company) and LV60 (Levensat sand, WBB Minerals, UK). These sand pack datasets are obtained by nuclear magnetic resonance scans and micro-computer tomography imaging by Talabi et al. (2009). Each sand pack dataset includes two-samples: F42B and F42C and LV60A and LV60C. All sand pack images have  $300^3$  voxels with resolution  $10.002 \mu m$ . Table 3 summarizes the sand pack data and Figure 12 shows their two-dimensional slice images.

Rock type	Sample	Porosity (%)	Grain surface area ( $M^2/m^3$ )
Unground silica F42	F42B	33.3	44,930
	F42C	33.1	45,760
Levensat sand LV60	LV60A	37.7	57,670
	LV60C	37.2	61,590

Table 3: Properties of sand pack data (Talabi et al., 2009).

Both rock types have similar porosity (a volume of pores divided by a total volume), but different grain surface area. In Figure 12, we see that the unground silica sand pack has larger-sized and circular-shaped grains compared to the Levensat sand pack. However,

it is difficult to compare structural or connectivity differences from the properties or the three-dimensional images.

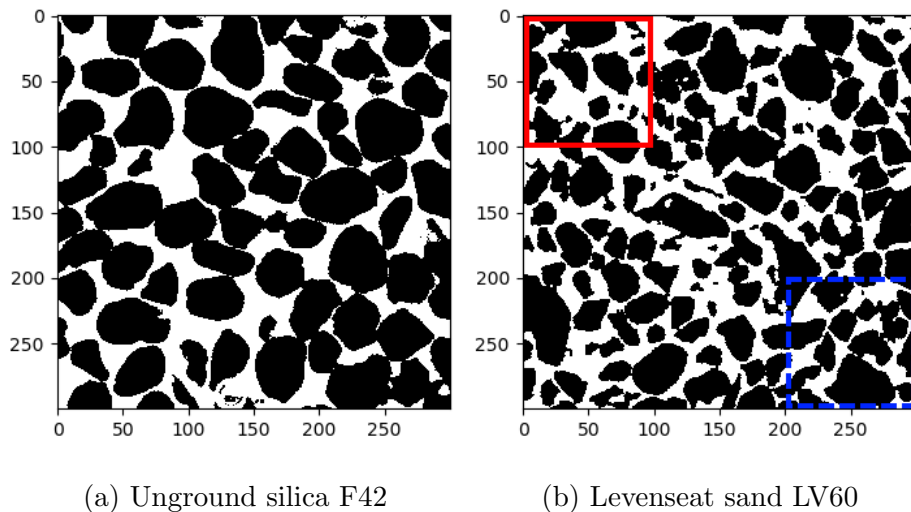


Figure 12: Two-dimensional slice images of two sand packs. Pores and grains are drawn as white and black elements. The red solid and the blue dotted box areas are two of the subregions that show large variabilities within the same rock image.

We compute persistent homology to extract structural and connectivity information of sand pack data. First, we take 27 subregion images of size  $100^3$  from each sand pack sample. The persistence diagrams are converted into persistence images using the soft arctangent weight.

We conduct hypothesis tests on three sets of data: between unground silica (F42B and F42C), between Levenseat sand (LV60A and LV60C), and between unground silica and Levenseat sand (F42B and LV60A). We compare two test procedures, the permutation and two-stage hypothesis tests.

The suggested two-stage hypothesis tests show larger structural and connectivity differences between different types of sand packs compared to the tests between the same type of rocks. Figure 13 shows two-stage hypothesis test results using the overall mean as a filter statistic, pooled variance  $t$ -tests. We see that there are elements that have small  $q$ -values for most of the dimensions and rock types. However, different types of rocks have larger areas of small  $q$ -values than the same type of rocks. This implies that various types of topological features account for differences between the two types of rocks. We report

the other test results using the overall standard deviation in Figure S4 in Supplementary Material.

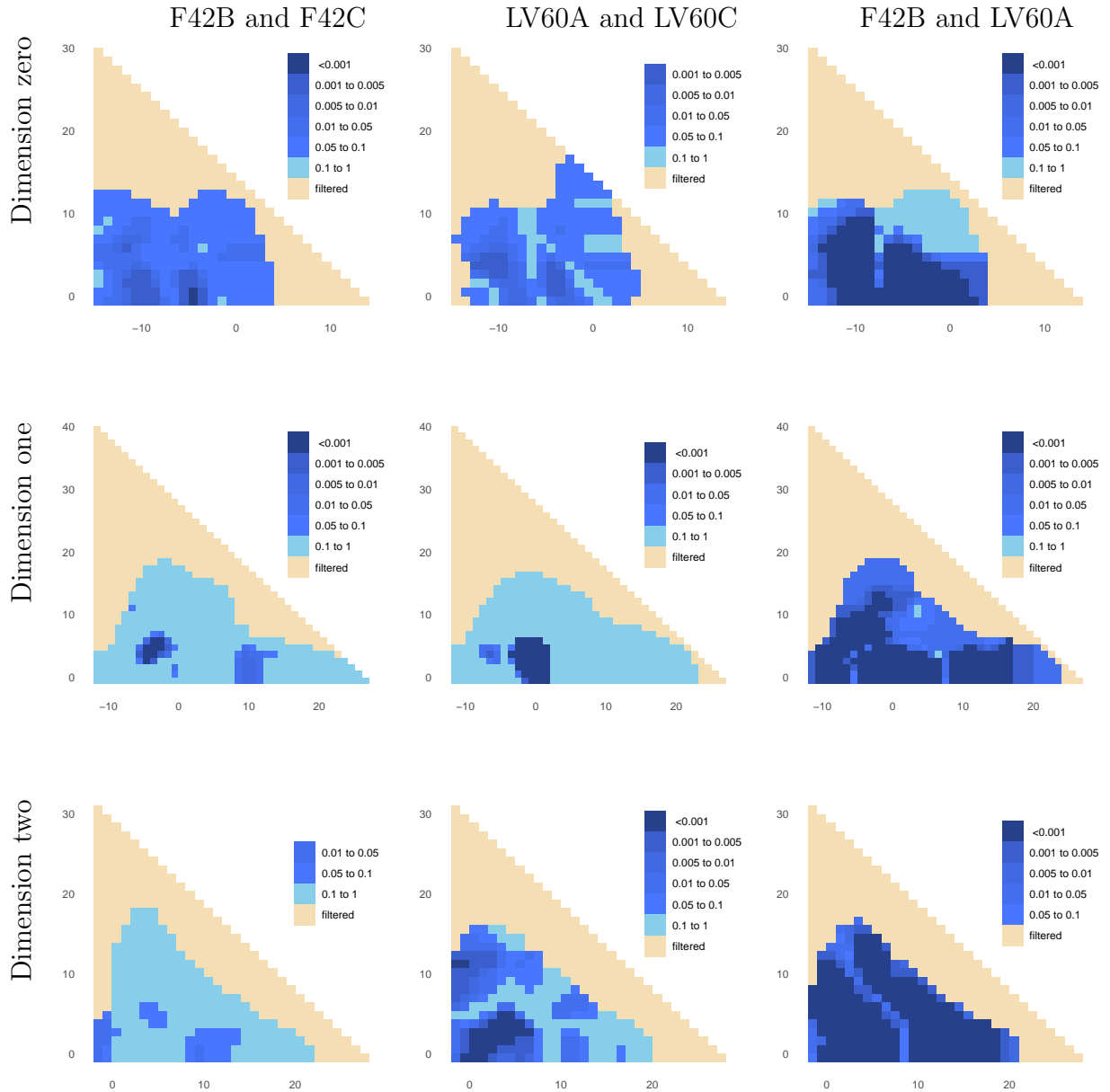


Figure 13:  $q$ -values of two-sample  $t$ -tests between F42 (first column), between LV60 (second column), and between F42 and LV60 (third column) for zero- (first row), one- (second row), two-dimensional (third row) persistence images.

Table 4 shows the permutation test results. We use  $N = 500$  permutations for dimension

zero and two, and  $N = 100$  for dimension one due to the computation time of pairwise distances (See later in this Section for a detailed discussion). Also, we use Wasserstein distance as a pairwise distance. For all cases, the computed permutation p-values are zero; every joint loss of shuffled labels  $L(G_{\text{shuffled}})$  is larger than the joint loss of the original unshuffled labels  $L(G_{\text{unshuffled}})$ . However, the differences of joint losses between unshuffled and shuffled labels are larger for the different types of rocks compared to the same type of rocks.

	F42B and F42C		LV60A and LV60C		F42A and LV60C	
	Unshuffled	Shuffled	Unshuffled	Shuffled	Unshuffled	Shuffled
Dimension 0	94.808	97.273	125.124	131.252	121.060	207.608
Dimension 1	222.994	228.117	274.708	329.955	254.671	528.637
Dimension 2	135.764	137.668	175.376	183.815	158.833	263.754

Table 4: Joint loss values of permutation tests. For shuffled labels, we report the mean of joint loss values.

We want to note that the small q-values and permutation p-values for both methods in the same type of rocks might be due to the small subregion size. The subregion size  $100^3$  is relatively small to represent the overall rock sample structure. The sampled subregions may not have similar structures and connectivity, even when they are taken from the same rock sample. For example, we observe that subregions from the same rock sample may have large variabilities themselves in Figure 12b; the subregion of size 100 by 100 in the top-left corner (in the red solid line box) has smaller sized and more sparse grains than the bottom-right corner subregion (in the blue dashed line box).

Both test approaches draw similar results, but the proposed two-stage hypothesis test approach has two advantages over the permutation test: interpretation and computational cost.

First, the two-stage hypothesis test enables detailed inference on the test results; it identifies which areas are the most different in the persistence diagrams. We see the areas with low q-values in Figure 13 that account for the differences. On the other hand, permutation tests do not provide such information. The permutation test only reports a single

permutation p-value that explains overall differences.

Second, the computational cost for the two-stage test is lower than the permutation test. Table 5 compares the running times of the two approaches for each dimension. For all computations, Intel Xeon 2.10 GHz CPUs are used. We see that the permutation test requires a substantially longer running time. Even if we consider the computation time for the vectorization process as part of the two-stage hypothesis test, the permutation test requires higher computation cost.

Method	Dimension	Number of cores used	Computation time
Two-stage test	Dimension 0	1	< 1 minute
	Dimension 1	1	< 1 minute
	Dimension 2	1	< 1 minute
Permutation test	Dimension 0 ( $N = 500$ )	40	$\approx 15$ hours
	Dimension 1 ( $N = 100$ )	50	$\approx 148$ hours
	Dimension 2 ( $N = 500$ )	40	$\approx 14$ hours

Table 5: Computation time of two hypothesis test methods for sand pack images.

Here, the computational bottleneck of the permutation test is the pairwise distance computation. For the point cloud simulation in Section 4.1, the number of features in a one-dimensional persistence diagram is 13 at maximum. On the other hand, we have up to 920 features in a one-dimensional persistence diagram for the sand pack analysis. Because we use the Hungarian algorithm to compute the Wasserstein distances ( $O(n_f^3)$  time complexity), the computational time is approximately 300,000 times longer for the sand pack analysis.

Note that we conduct the test on a small number of persistence diagrams, 27 persistence diagrams for each group. If we run the permutation test on a large number of persistence diagrams, the computational cost will further increase.

## 5 Discussion

This paper presents a two-stage hypothesis test for a vectorized persistence diagram that consists of filtering and testing steps. Our approach enables a better interpretation by providing specific regions on the persistence diagram that contribute the most to any observed differences. Also, the proposed test procedure is less costly from a computational perspective compared to the permutation test of Robinson and Turner (2017).

On the other hand, the two-stage test for vectorized persistence diagrams could lead to a potential problem of giving a researcher too many degrees of freedom. The proposed method provides a flexible way to conduct a hypothesis test for persistent homology by implementing weights and smoothing. The results in Figure 9 indicate that the weights play an important role for a successful result in revealing the differences between persistence diagrams. However, the weight selection process itself is still an unanswered question. Also, selecting the filter threshold  $C$  can be an issue. In practice, one may choose the filter threshold heuristically using an empirical distribution of filter statistics. In the future, we plan to explore systematical methods to select the weights and parameters.

## References

- Adams, H., Emerson, T., Kirby, M., Neville, R., Peterson, C., Shipman, P., Chepushtanova, S., Hanson, E., Motta, F., and Ziegelmeier, L. (2017), “Persistence Images: A Stable Vector Representation of Persistent Homology,” *Journal of Machine Learning Research*, 18, 1–35.
- Adcock, A., Carlsson, E., and Carlsson, G. (2016), “The ring of algebraic functions on persistence bar codes,” *Homology, Homotopy and Applications*, 18, 381–402.
- Bendich, P., Chin, S. P., Clark, J., Desena, J., Harer, J., Munch, E., Newman, A., Porter, D., Rouse, D., Strawn, N., and Watkins, A. (2016a), “Topological and statistical behavior classifiers for tracking applications,” *IEEE Transactions on Aerospace and Electronic Systems*, 52, 2644–2661.

- Bendich, P., Marron, J. S., Miller, E., Pieloch, A., and Skwerer, S. (2016b), “Persistent Homology Analysis of Brain Artery Trees,” *Annals of Applied Statistics*, 10, 198–218.
- Benjamini, Y. and Hochberg, Y. (1995), “Controlling the False Discovery Rate: A Practical and Powerful Approach to Multiple Testing,” *Journal of the Royal Statistical Society: Series B (Statistical Methodological)*, 57, 289–300.
- (2000), “On the Adaptive Control of the False Discovery Rate in Multiple Testing with Independent Statistics,” *Journal of Educational and Behavioral Statistics*, 25, 60–83.
- Benjamini, Y., Krieger, A. M., and Yekutieli, D. (2006), “Adaptive linear step-up procedures that control the false discovery rate,” *Biometrika*, 93, 491–507.
- Benjamini, Y. and Yekutieli, D. (2001), “The control of the false discovery rate in multiple testing under dependency,” *Annals of Statistics*, 29, 1165–1188.
- Bernab, Y. and Bruderer, C. (1998), “Effect of the variance of pore size distribution on the transport properties of heterogeneous networks,” *Journal of Geophysical Research: Solid Earth*, 103, 513–525.
- Berry, E., Chen, Y.-C., Cisewski-Kehe, J., and Fasy, B. T. (2020), “Functional summaries of persistence diagrams,” *Journal of Applied and Computational Topology*, 4, 211–262.
- Billard, L. and Diday, E. (2006), *Symbolic Data Analysis : Conceptual Statistics and Data Mining*, Wiley Series in Computational Statistics, John Wiley & Sons Inc.
- Bourgon, R., Gentleman, R., and Huber, W. (2010), “Independent filtering increases detection power for high-throughput experiments,” *Proceedings of the National Academy of Sciences*, 107, 9546–9551.
- Bubenik, P. (2015), “Statistical Topological Data Analysis Using Persistence Landscapes,” *Journal of Machine Learning Research*, 16, 77–102.
- Cang, Z. and Wei, G.-W. (2017), “TopologyNet: Topology based deep convolutional and multi-task neural networks for biomolecular property predictions,” *PLOS Computational Biology*, 13, 1–27.

- Carlsson, G. (2009), “Topology and data,” *Bulletin of the American Mathematical Society*, 46, 255–308.
- Cericola, C., Johnson, I. J., Kiers, J., Krock, M., Purdy, J., and Torrence, J. (2018), “Extending hypothesis testing with persistent homology to three or more groups,” *Involve: A Journal of Mathematic*, 11, 27–51.
- Chazal, F., Fasy, B., Lecci, F., Michel, B., Rinaldo, A., Rinaldo, A., and Wasserman, L. (2017), “Robust Topological Inference: Distance to a Measure and Kernel Distance,” *Journal of Machine Learning Research*, 18, 58455884.
- Chen, Y.-C., Wang, D., Rinaldo, A., and Wasserman, L. (2015), “Statistical Analysis of Persistence Intensity Functions,” *arXiv e-prints*.
- Dlotko, P. (2015), “Cubical complex,” in *GUDHI User and Reference Manual*, GUDHI Editorial Board.
- Du, L. and Zhang, C. (2014), “Single-index modulated multiple testing,” *Annals of Statistics*, 42, 1262–1311.
- Edelsbrunner, H. and Harer, J. (2008), “Persistent Homology - a Survey,” *Contemporary mathematics*, 453, 257–282, surveys on Discrete and Computational Geometry: Twenty Years Later. Providence, IMS.
- (2010), *Computational topology : an introduction.*, Providence, R.I. : American Mathematical Society, c2010.
- Fan, J., Han, X., and Gu, W. (2012), “Estimating False Discovery Proportion Under Arbitrary Covariance Dependence,” *Journal of the American Statistical Association*, 107, 1019–1035, pMID: 24729644.
- Fasy, B. T., Kim, J., Lecci, F., Maria, C., and Rouvreau, V. (2019), *TDA: Statistical Tools for Topological Data Analysis*, r package version 1.6.5.
- Fasy, B. T., Lecci, F., Rinaldo, A., Wasserman, L., Balakrishnan, S., and Singh, A. (2014), “Confidence sets for persistence diagrams,” *Annals of Statistics*, 42, 2301–2339.

- Genovese, C. R., Perone-Pacifico, M., Verdinelli, I., and Wasserman, L. (2012), “Manifold estimation and singular deconvolution under Hausdorff loss,” *Annals of Statistics*, 40, 941–963.
- Ghrist, R. (2008), “Barcodes: The Persistent Topology of Data,” *Bulletin of the American Mathematical Society*, 45, 61–75.
- Gretton, A., Borgwardt, K. M., Rasch, M., Schölkopf, B., and Smola, A. J. (2006), “A kernel method for the two-sample problem,” *Proceedings of the 19th International Conference on Neural Information Processing Systems*, 513–520.
- Gretton, A., Borgwardt, K. M., Rasch, M. J., Schölkopf, B., and Smola, A. (2012), “A Kernel Two-sample Test,” *Journal of Machine Learning Research*, 13, 723–773.
- Guo, W. and Romano, J. P. (2017), “Analysis of error control in large scale two-stage multiple hypothesis testing,” *arXiv e-prints*, arXiv:1703.06336.
- Hackstadt, A. J. and Hess, A. M. (2009), “Filtering for increased power for microarray data analysis,” *BMC bioinformatics*, 10, doi:10.1186/1471-2105-10-11.
- Hatcher, A. (2002), *Algebraic Topology*, Cambridge University Press.
- Hiraoka, Y., Nakamura, T., Hirata, A., Escolar, E. G., Matsue, K., and Nishiura, Y. (2016), “Hierarchical structures of amorphous solids characterized by persistent homology,” *Proceedings of the National Academy of Sciences*, 113, 7035–7040.
- Hochberg, Y. and Tamhane, A. C. (1987), *Multiple Comparison Procedures*, John Wiley & Sons, Inc.
- Hommel, J., Coltman, E., and Class, H. (2018), “PorosityPermeability Relations for Evolving Pore Space: A Review with a Focus on (Bio-)geochemically Altered Porous Media,” *Transport in Porous Media*.
- Ignatiadis, N., Klaus, B., Zaugg, J., and Huber, W. (2016), “Data-driven hypothesis weighting increases detection power in big data analytics,” *Nature Methods*, 13, 577580.

- Imperial College London (2015), “Pore Scale Modelling group: Micro-CT images and networks,” Retrieved from <http://www.imperial.ac.uk/engineering/departments/earth-science/research/research-groups/perm/research/pore-scale-modelling/micro-ct-images-and-networks>.
- Kališnik, S. (2019), “Tropical coordinates on the space of persistence barcodes,” *Foundations of Computational Mathematics*, 19, 101–129.
- Kerber, M., Morozov, D., and Nigmatov, A. (2017), “Geometry helps to compare persistence diagrams,” *Journal of Experimental Algorithmics*, 22, 1–20.
- Kim, K. I. and van de Wiel, M. A. (2008), “Effects of dependence in high-dimensional multiple testing problems,” *BMC bioinformatics*, 9, 114.
- Kooperberg, C. and LeBlanc, M. (2008), “Increasing the power of identifying gene x gene interactions in genome-wide association studies,” *Genetic Epidemiology*, 32, 255–263.
- Kusano, G. (2019), “On the expectation of a persistence diagram by the persistence weighted kernel,” *Japan Journal of Industrial and Applied Mathematics*, 36, 861–892.
- Kusano, G., Fukumizu, K., and Hiraoka, Y. (2016), “Persistence weighted Gaussian kernel for topological data analysis,” *Proceedings of the 33rd International Conference on International Conference on Machine Learning*, 48, 2004–2013.
- Maroulas, V., Nasrin, F., and Oballe, C. (2019), “Bayesian inference for persistent homology,” *arXiv e-prints*, arXiv:1901.02034.
- Marron, J. S. and Alonso, A. M. (2014), “Overview of object oriented data analysis,” *Biometrical Journal*, 56, 732–753.
- McClintick, J. N. and Edenberg, H. J. (2006), “Effects of filtering by present call on analysis of microarray experiments,” *BMC bioinformatics*, 7, doi:10.1186/1471-2105-7-49.
- Mieth, B., Kloft, M., Rodríguez, J. A., Sonnenburg, S., Vobruba, R., Morcillo-Suárez, C., Farré, X., Marigorta, U. M., Fehr, E., Dickhaus, T., Blanchard, G., Schunk, D., Navarro, A., and Müller, K.-R. (2016), “Combining multiple hypothesis testing with machine

- learning increases the statistical power of genome-wide association studies,” *Scientific Reports*, 6, doi:10.1038/srep36671.
- Munkres, J. (1957), “Algorithms for the assignment and transportation problems,” *Journal of the Society for Industrial and Applied Mathematics*, 5, 32–38.
- Murcray, C. E., Lewinger, J. P., and Gauderman, W. J. (2008), “Gene-environment interaction in genome-wide association studies,” *American Journal of Epidemiology*, 169, 219–226.
- Obayashi, I., Hiraoka, Y., and Kimura, M. (2018), “Persistence diagrams with linear machine learning models,” *Journal of Applied and Computational Topology*, 1, 421–449.
- Ramsay, J. and Silverman, B. W. (2005), *Functional Data Analysis*, New York, NY: Springer-Verlag.
- Reininghaus, J., Huber, S. M., Bauer, U., and Kwitt, R. (2015), “A stable multi-scale kernel for topological machine learning,” *2015 IEEE Conference on Computer Vision and Pattern Recognition*, 4741–4748, doi:10.1109/CVPR.2015.7299106.
- Robins, V., Saadatfar, M., Delgado-Friedrichs, O., and Sheppard, A. P. (2016), “Percolating length scales from topological persistence analysis of micro-CT images of porous materials,” *Water Resources Research*, 52, 315–329.
- Robins, V. and Turner, K. (2016), “Principal component analysis of persistent homology rank functions with case studies of spatial point patterns, sphere packing and colloids,” *Physica D: Nonlinear Phenomena*, 334, 99–117.
- Robinson, A. and Turner, K. (2017), “Hypothesis testing for topological data analysis,” *Journal of Applied and Computational Topology*, 1, 241–261.
- Stevens, J. R., Al Masud, A., and Suyundikov, A. (2017), “A comparison of multiple testing adjustment methods with block-correlation positively-dependent tests,” *PLOS ONE*, 12, 1–12.

- Storey, J. D. (2002), “A direct approach to false discovery rates,” *Journal of the Royal Statistical Society: Series B (Statistical Methodology)*, 64, 479–498.
- Talabi, O., AlSayari, S., Iglauer, S., and Blunt, M. J. (2009), “Pore-scale simulation of NMR response,” *Journal of Petroleum Science and Engineering*, 67, 168–178.
- Tritchler, D., Parkhomenko, E., and Beyene, J. (2009), “Filtering Genes for Cluster and Network Analysis,” *BMC Bioinformatics*, 10, doi:10.1186/1471-2105-10-193.
- Vejdemo-Johansson, M. and Mukherjee, S. (2018), “Multiple testing with persistent homology,” *arXiv e-prints*, arXiv:1803.08269.
- Xiong, Q., Baychev, T. G., and Jivkov, A. P. (2016), “Review of pore network modelling of porous media: Experimental characterisations, network constructions and applications to reactive transport,” *Journal of Contaminant Hydrology*, 192, 101 – 117.

## Supplementary Material

---

**Algorithm S1** Permutation test (Robinson and Turner, 2017)

---

**Input:** Persistence diagrams, given group label  $G_{\text{unshuffled}}$ , number of repetitions  $N$ , joint loss function  $L$

**Output:** Permutation p-value  $Z$

Compute  $L(G_{\text{unshuffled}})$

Create an empty vector  $L$  of size  $N$

**for**  $i = 1 \rightarrow N$  **do**

    Randomly generate shuffled group label  $G_{\text{shuffled}}^i$

$L[i] \leftarrow L(G_{\text{shuffled}}^i)$

**end for**

$Z \leftarrow \text{sum}(L < L(G_{\text{unshuffled}}))/N$

---

---

**Algorithm S2** Two-stage hypothesis test procedure

---

**Input:** Array of  $n$  vectorized persistence diagrams  $V_{\{m^2 \times n\}}$ , given label  $G_{\text{given}} = \{I, J\}$ , threshold  $C$

**Output:** P-values  $Z$

Create vector  $v_x, v_y$  of size  $m^2$  that correspond to  $x$  and  $y$  locations of  $V$

$V \leftarrow V[v_x \geq v_y, ]$

Create an empty vector  $T$  of size  $\frac{m(m+1)}{2}$

**for**  $i = 1 \rightarrow \frac{m(m+1)}{2}$  **do**

$T[i] \leftarrow$  filter statistic of  $i$ th element of  $V$

**end for**

$t_C \leftarrow C^{\text{th}}$  percentile of  $T$

$V \leftarrow V[V > t_C, ]$

Create an empty vector  $Z$  of size  $nrow(V)$

**for**  $j = 1 \rightarrow nrow(V)$  **do**

$v_1 \leftarrow V[j, I]$

$v_2 \leftarrow V[j, J]$

    Conduct a hypothesis test using  $v_1$  and  $v_2$  and store p-value in  $Z[j]$

**end for**

Apply multiple testing adjustment procedure to  $Z$

---

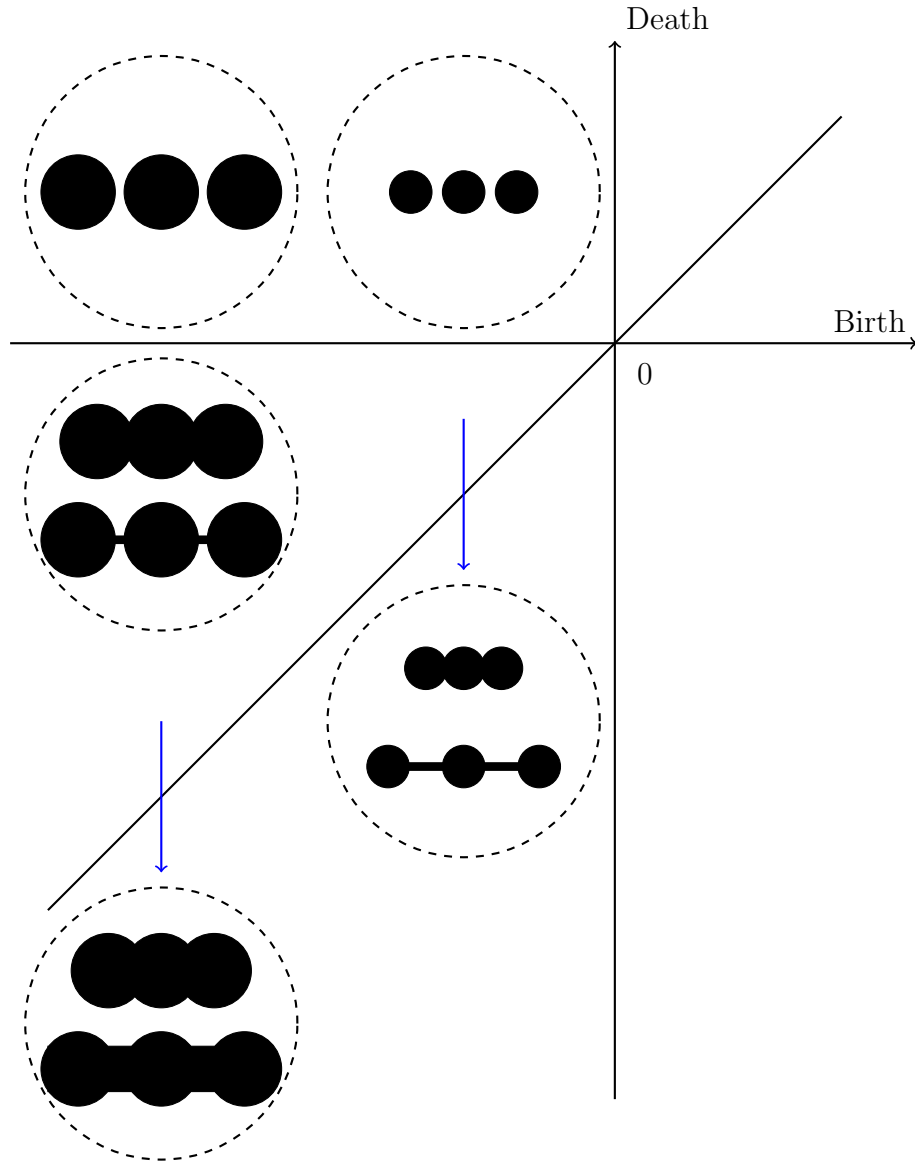


Figure S1: Examples of topological features of two-dimensional binary rock images (in dashed circles) and where they appear in the dimension 0 persistence diagram. The dimension 0 persistent diagrams reveal the size of grains and connectivity. For example, larger(smaller) grains have larger(smaller) negative birth values and closely(weakly) connected grains have large(small) negative death values. Also, connected(not connected) grains have negative(positive) death values, so they are recorded on the third(second) quadrant of the persistence diagram. Grains and pores are colored in black and white, respectively.

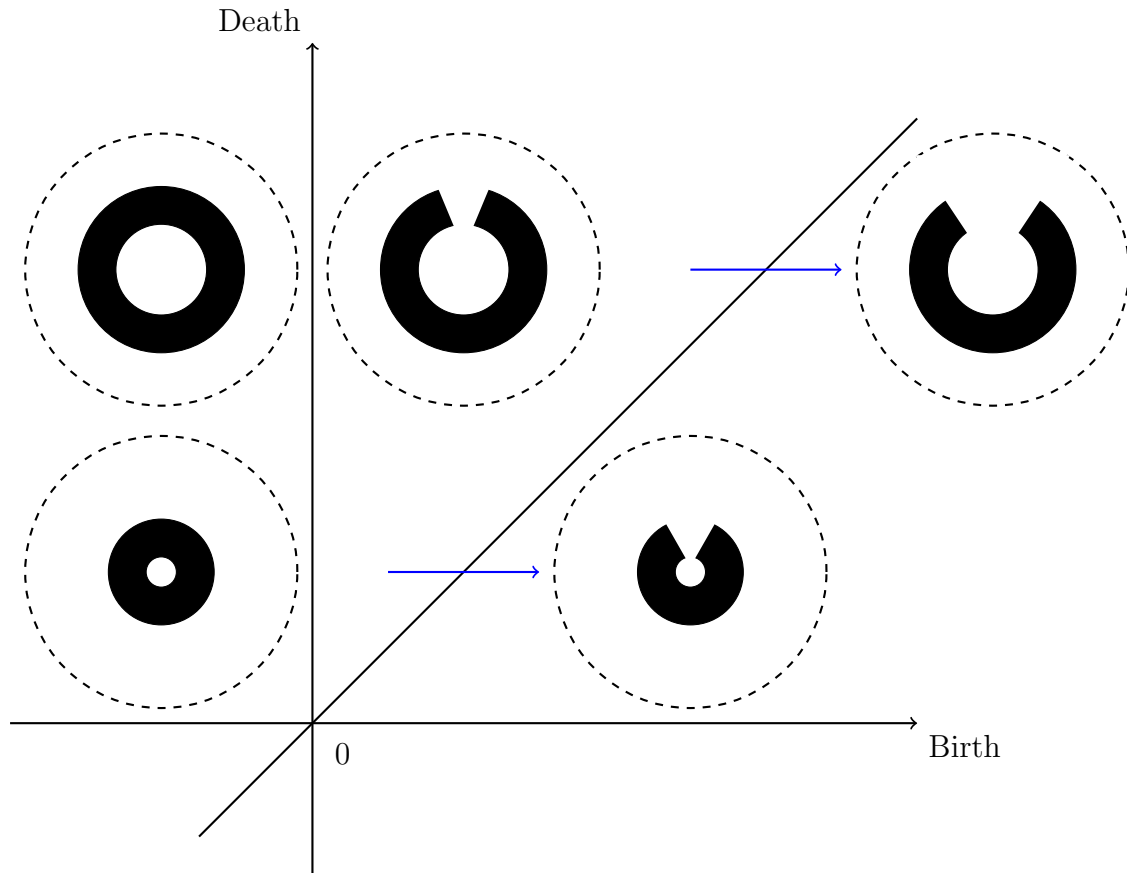


Figure S2: Examples of topological features of two-dimensional binary rock images (in dashed circles) and where they appear in the dimension 1 persistence diagram. The dimension 1 persistent diagrams show the structure of grains and pores. The second quadrant (negative birth and positive death) is related to pores trapped inside of grains and the birth(death) value is proportional to the size of the corresponding grain(pore). On the other hand, the first quadrant (positive birth and death) represents the grains look like a horseshoe or broken ring. Grains and pores are colored in black and white, respectively.

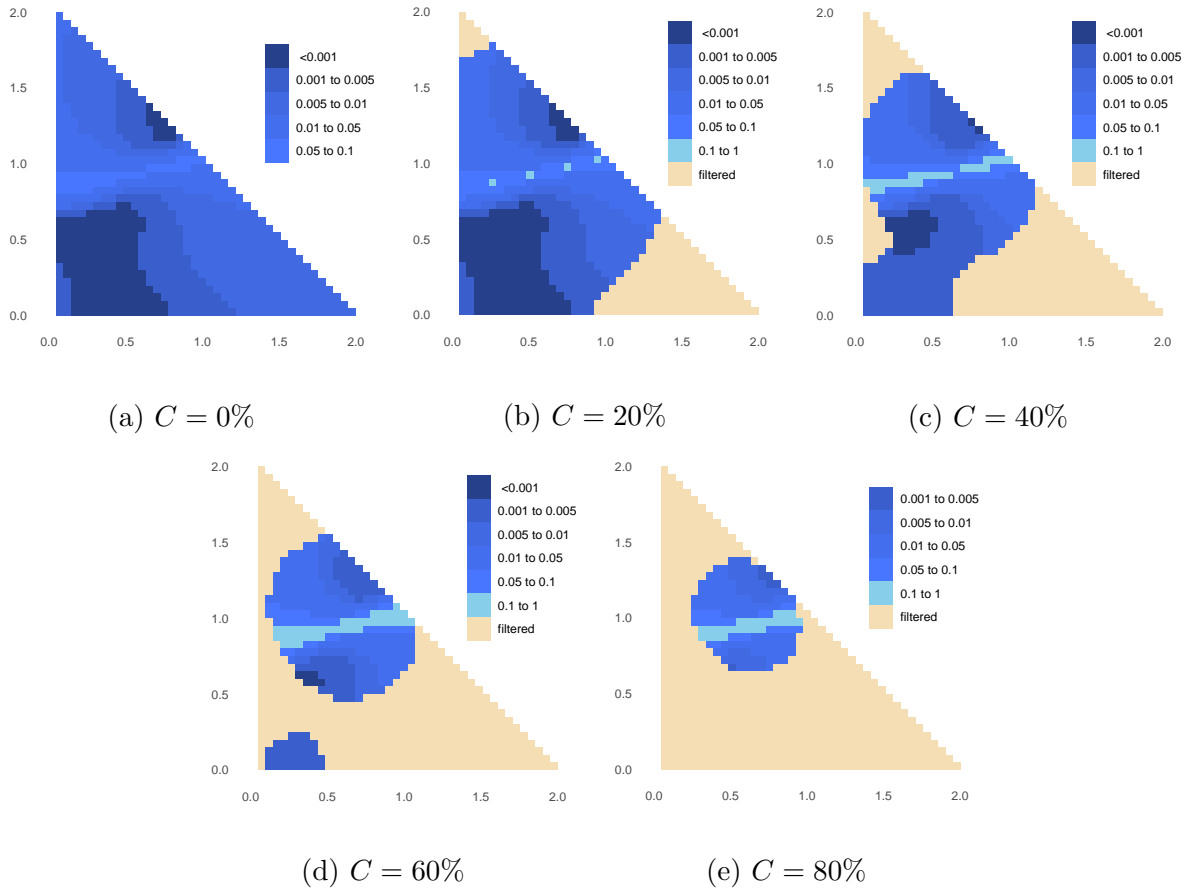


Figure S3: q-values of two sample t-tests. The overall sample mean is used as the filter statistic.

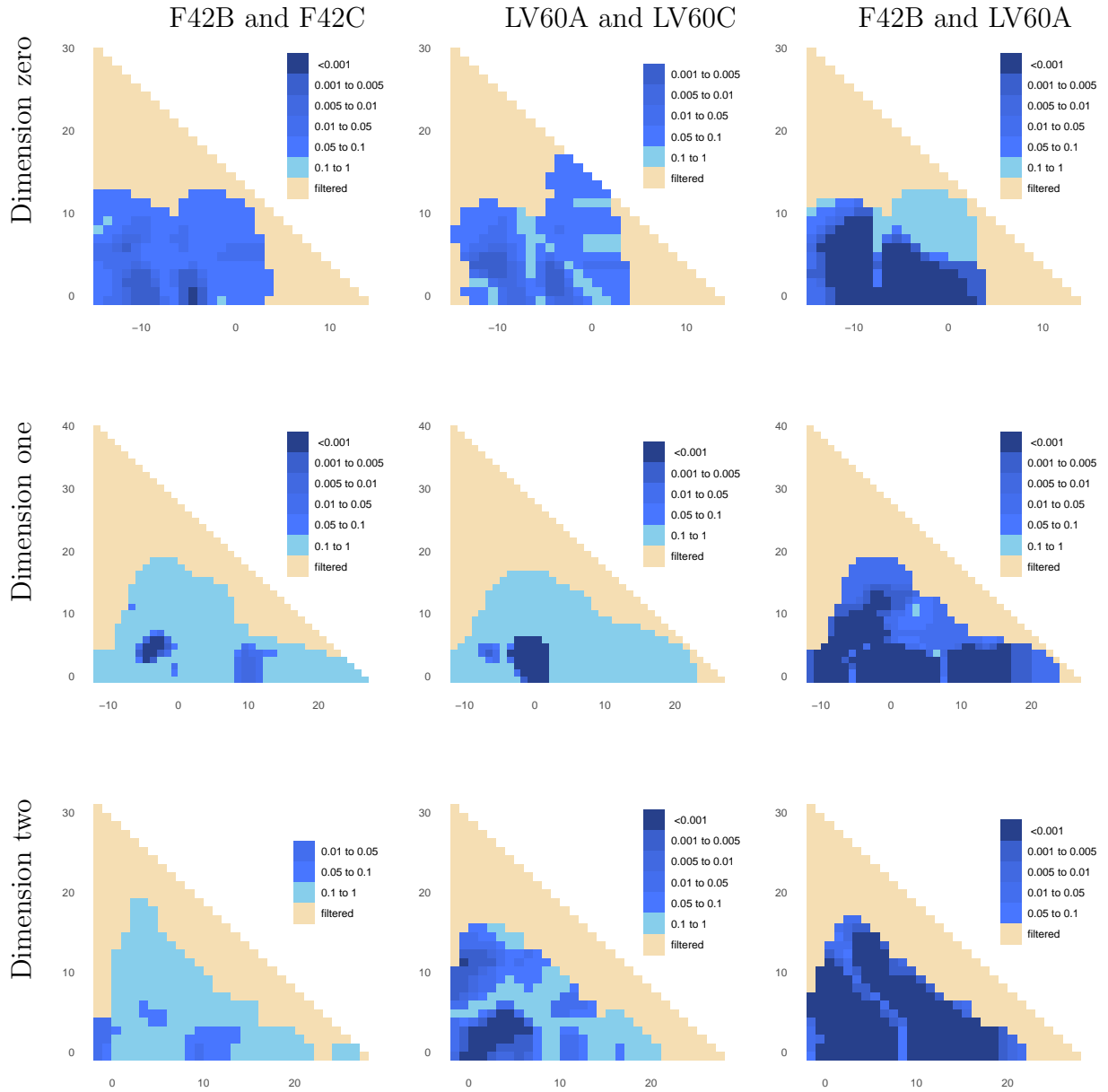


Figure S4: q-values of two-sample t-tests between F42 (first column), between LV60 (second column), and between F42 and LV60 (third column) for zero- (first row), one- (second row), two-dimensional (third row) persistence images. We filter using overall standard deviation.

Filter Statistics	Threshold	Noise			
		0.05	0.10	0.15	0.20
Overall Sample Mean	0%	0.996	0.750	0.372	0.226
	20%	0.998	0.770	0.384	0.236
	40%	0.998	0.796	0.432	0.266
	60%	0.998	0.840	0.514	0.326
	80%	0.992	0.780	0.332	0.158
Overall Sample Standard Deviation	0%	0.996	0.750	0.372	0.226
	20%	0.998	0.770	0.390	0.238
	40%	0.996	0.792	0.438	0.280
	60%	0.994	0.728	0.450	0.310
	80%	0.974	0.632	0.288	0.170

Table S1: Powers of multiple t-tests on persistence images with constant weight at significance level  $\alpha = 0.05$

Filter Statistics	Threshold	Noise			
		0.05	0.10	0.15	0.20
Overall Sample Mean	0%	0.996	0.698	0.316	0.164
	20%	0.998	0.712	0.322	0.168
	40%	0.998	0.732	0.364	0.184
	60%	0.984	0.698	0.382	0.234
	80%	0.856	0.486	0.352	0.226
Overall Sample Standard Deviation	0%	0.996	0.698	0.316	0.164
	20%	0.998	0.708	0.326	0.170
	40%	0.992	0.712	0.374	0.212
	60%	0.976	0.678	0.404	0.256
	80%	0.838	0.538	0.308	0.166

Table S2: Powers of multiple t-tests on persistence images with soft arctangent weight at significance level  $\alpha = 0.05$

Filter Statistics	Threshold	Noise			
		0.05	0.10	0.15	0.20
Overall Sample Mean	0%	0.994	0.632	0.284	0.126
	20%	0.996	0.646	0.296	0.136
	40%	0.990	0.604	0.300	0.146
	60%	0.920	0.500	0.272	0.156
	80%	0.824	0.414	0.220	0.124
Overall Sample Standard Deviation	0%	0.994	0.632	0.284	0.126
	20%	0.994	0.636	0.296	0.142
	40%	0.944	0.554	0.300	0.164
	60%	0.796	0.444	0.296	0.192
	80%	0.588	0.336	0.204	0.118

Table S3: Powers of multiple t-tests on persistence images with hard arctangent weight at significance level  $\alpha = 0.05$

Filter Statistics	Threshold	Noise			
		0.05	0.10	0.15	0.20
Overall Sample Mean	0%	0.502	0.100	0.054	0.040
	20%	0.356	0.124	0.068	0.042
	40%	0.384	0.142	0.080	0.044
	60%	0.448	0.146	0.094	0.066
	80%	0.532	0.132	0.092	0.056
Overall Sample Standard Deviation	0%	0.502	0.100	0.054	0.040
	20%	0.548	0.112	0.060	0.050
	40%	0.564	0.118	0.062	0.058
	60%	0.586	0.122	0.084	0.064
	80%	0.580	0.126	0.070	0.066

Table S4: Powers of multiple t-tests on persistence images with linear weight at significance level  $\alpha = 0.05$